

Taming the Sigmoid Bottleneck: Provably Argmaxable Sparse Multi-Label Classification

Andreas Grivas¹, Antonio Vergari², Adam Lopez^{†1}

¹ Institute for Language, Cognition, and Computation

² Institute for Adaptive and Neural Computation

School of Informatics, University of Edinburgh

{agrivas, avergari, alopez}@ed.ac.uk

Abstract

Sigmoid output layers are widely used in multi-label classification (MLC) tasks, in which multiple labels can be assigned to any input. In many practical MLC tasks, the number of possible labels is in the thousands, often exceeding the number of input features and resulting in a *low-rank* output layer. In multi-class classification, it is known that such a low-rank output layer is a bottleneck that can result in *unargmaxable* classes: classes which cannot be predicted for any input. In this paper, we show that for MLC tasks, the analogous *sigmoid bottleneck* results in exponentially many unargmaxable label combinations. We explain how to detect these unargmaxable outputs and demonstrate their presence in three widely used MLC datasets. We then show that they can be prevented in practice by introducing a Discrete Fourier Transform (DFT) output layer, which guarantees that all sparse label combinations with up to k active labels are argmaxable. Our DFT layer trains faster and is more parameter efficient, matching the F1@k score of a sigmoid layer while using up to 50% fewer trainable parameters. Our code is publicly available at <https://github.com/andreasgrv/sigmoid-bottleneck>.

1 Introduction

Sigmoid classifiers for Multi-Label Classification (MLC) are simple to implement: just append a linear layer with sigmoid activations to your neural feature encoder of choice. They are widely used in neural MLC with thousands of output labels; applications include clinical coding (Mullenbach et al. 2018), image classification (Baruch et al. 2020), fine-grained entity typing (Choi et al. 2018) and protein function prediction (Kulmanov and Hoehndorf 2019). Moreover, they are the default for MLC in frameworks such as Scikit-learn (Pedregosa et al. 2011) and Keras (Paul and Rakshit 2014). In this paper we highlight an overlooked weakness of this layer. If, as is common for computational efficiency, we make the number of features smaller than the number of labels, the result is a **Bottlenecked Sigmoid Layer (BSL)**, in which *exponentially many label combinations cannot be predicted irrespective of input*. We say that such label combinations are **unargmaxable** (Grivas, Bogoychev, and Lopez 2022). Fig. 1a illustrates how a BSL can give rise to

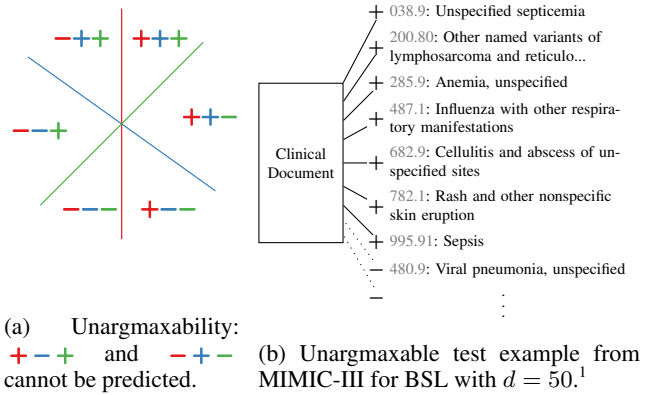


Figure 1: **Problem: When we have more labels (n) than features (d), some label combinations are unargmaxable**, i.e. impossible to predict. Left: in a $d = 2$ feature space with $n = 3$ classification hyperplanes through the origin, only 6 out of 8 label combinations can be predicted.² Right: in the MIMIC-III clinical coding dataset with $n = 8921$ and $d = 50$, a classifier is unable to correctly predict the 7 depicted ICD-9 code labels as active (+) and the remaining labels as inactive (-).

unargmaxability even in low dimensions, with only two features and three labels.

But unargmaxable label combinations are only a problem if our application requires those combinations. As we show in this paper, they often do. For example, in the safety-critical application of clinical coding (see Section 5), unargmaxability can make it impossible to label a report with a specific combination of findings, as illustrated with a real example in Fig. 1b. This would be surprising and unacceptable to users of the system when such label combinations do indeed occur in data. Since BSLs are widely used, it is critical for developers and users of a model to be aware of this problem and to be able to guarantee that all meaningful outputs for a task are argmaxable.

Previous work has shown that bottlenecked output layers

¹There are also unargmaxable test examples for $d = 100$ and $d = 200$, we chose this example for clarity as it had less labels.

²The hyperplanes will not meet at the origin if the BSL includes a bias term, but this is mathematically equivalent to adding a single (fixed) input feature: the problem persists.

[†]Joint supervision.

have restrictions on expressivity, but focused only on multi-class classification (Yang et al. 2018; Ganea et al. 2019) and not MLC. But for multi-class classification, the consequences are minor: classes can be unargmaxable in theory (Demeter, Kimmel, and Downey 2020) but rarely are in practice (Grivas, Bogoychev, and Lopez 2022). In MLC, we will show that exponentially many label combinations are unargmaxable, and as we have already seen in Fig. 1b, meaningful outputs can be unargmaxable. While a BSL can in principle learn to represent any particular output, it comes with no guarantees. And although we can obtain post hoc guarantees by verifying whether specific meaningful outputs are argmaxable, there may be too many outputs to check exhaustively. To sidestep this limitation, we show how to construct an output layer that guarantees that meaningful outputs are argmaxable by construction. To do so, we provide guarantees for a superset of outputs: those with up to k active labels, where we choose k based on the statistics of the dataset. This is possible since for most MLC tasks k is bounded (Jain et al. 2019), either empirically (e.g. $k=80$ for MIMIC-III) or by construction (e.g. $k=50$ for BioASQ (Tsatsaronis et al. 2015)).

In summary, our contributions are: **i**) We formalize the argmaxability problem for MLC and expose the limitations of BSLs which are widely used in practice (Section 2); **ii**) We provide ways of verifying if a label combination is argmaxable for a model (Section 3) and show that for three widely used MLC datasets BSLs can have unargmaxable test set label combinations (Section 5). **iii**) We prove that this need not be the case; we can guarantee that any output with up to k active labels is argmaxable by constraining the output layer parametrisation to a family of matrices. The Discrete Fourier Transform (DFT) matrix is in this family and we use it to parametrise our DFT layer, an efficient replacement output layer with such guarantees (Section 4). **iv**) Through experiments on three MLC datasets we show that our DFT layer guarantees that meaningful outputs are argmaxable while converging faster and being more parameter efficient than a BSL (Section 5).

2 Multi-label Classification

We consider a MLC model that predicts a complete label assignment $\mathbf{y} \in \{+, -\}^n$ for a label vocabulary of size n , and where each $y_i \in \{+, -\}$ denotes if a single label is active (+) or inactive (-). Many neural MLC models for problems with large label vocabularies employ an output layer that is linear, e.g., for fine-grained entity typing (Choi et al. 2018), protein function prediction (Kulmanov and Hoehndorf 2019), clinical coding (Mullenbach et al. 2018) and multi-label image classification (Baruch et al. 2020).

Bottlenecked Sigmoid Layers. A linear sigmoid layer takes as input a feature vector $\mathbf{x} \in \mathbb{R}^d$ and predicts \mathbf{y} by assuming that all labels are independent given \mathbf{x} . The idea is that a powerful encoder does the “heavy lifting” and projects inputs to meaningful embeddings in \mathbb{R}^d such that they can be easily separated by n different hyperplanes. When n is large, due to computational constraints it is popular to realize such a layer as a *Bottlenecked Sigmoid Layer* (BSL)

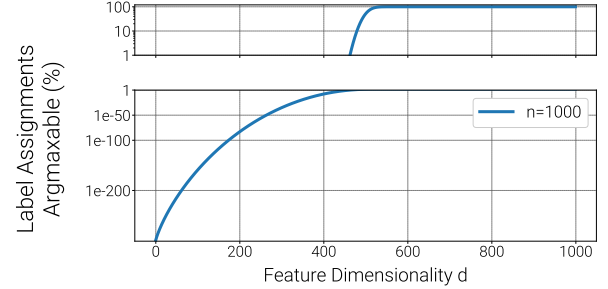


Figure 2: **The number of argmaxable label configurations shrinks exponentially as $d \ll n$.** We plot the percentage of the 2^{1000} label combinations that are argmaxable for a BSL with $n = 1000$ labels as we vary the feature dimensionality d . For $d \ll n$ there is a fast dip when $d < 500$ (see left side).

which is parametrized by a low-rank $\mathbf{W} \in \mathbb{R}^{n \times d}$ and associates with each label the probability $P(\mathbf{y}_i \mid \mathbf{x}) = \sigma(\mathbf{w}_i^\top \mathbf{x})$ if $\mathbf{y}_i = +$ and $1 - \sigma(\mathbf{w}_i^\top \mathbf{x})$ otherwise. Here, σ is the logistic sigmoid and \mathbf{w}_i is the weight vector of the i -th classifier (hyperplane), i.e., the i^{th} row of \mathbf{W} . Note that all \mathbf{w}_i see the same shared \mathbf{x} . We focus on such a setup and discuss its limitations because it is the default in mainstream ML libraries such as scikit-learn (Pedregosa et al. 2011) and largely used as a simple classifier (Mullenbach et al. 2018; Baruch et al. 2020; Kulmanov and Hoehndorf 2019). In the following, we will denote a whole multi-label classifier by the parametrization of its last layer, e.g., by saying “a classifier \mathbf{W} ”, as our analysis is agnostic to the feature encoder.

Argmaxable Label Assignments. Making a prediction with a BSL boils down to predicting every label independently by computing $\mathbf{y}_i^* = \operatorname{argmax}_{\mathbf{y}_i} P(\mathbf{y}_i \mid \mathbf{x})$. This is equivalent to taking the sign of the logits of the i -th classifier, i.e., computing $\mathbf{y}_i^* = \operatorname{sign}(\mathbf{w}_i^\top \mathbf{x})$ where $\operatorname{sign}(\mathbf{z}_i) = +$ if $\mathbf{z}_i > 0$ and $-$ if $\mathbf{z}_i < 0$. Therefore, $\mathbf{y}^* = \operatorname{sign}(\mathbf{W}\mathbf{x})$.

Definition 1. A label assignment \mathbf{y} is **argmaxable** for a classifier \mathbf{W} if there exists an input \mathbf{x} for which thresholding the output probabilities using the argmax decision rule $\operatorname{sign}(P(\mathbf{y}_i = + \mid \mathbf{x}) - \frac{1}{2})$ produces \mathbf{y}_i .³, i.e., \mathbf{y} is argmaxable $\iff \exists \mathbf{x} : \operatorname{sign}(\mathbf{W}\mathbf{x}) = \mathbf{y}$.

From a geometric perspective, we can interpret the n rows of \mathbf{W} as the normal vectors, \mathbf{w}_i , of n hyperplanes that tessellate feature space into regions. We can identify each region by assigning it a sign vector which identifies on which side of each hyperplane it is (Fig. 1, left). Under this view, a label assignment \mathbf{y} is argmaxable if the halfspaces intersect in such a way that the corresponding region is formed. For example, the region  is formed as an intersection of the negative halfspaces. For a classifier parameterized by a full rank $\mathbf{W} \in \mathbb{R}^{n \times n}$, all 2^n label combinations are argmaxable. However, since $d \ll n$ in many real-world applications, as discussed in Section 1, \mathbf{W} will be low rank, and therefore only a (small) subset of label combinations is argmaxable.

³Due to monotonicity of sigmoid $\sigma(a) > \frac{1}{2} \iff a > 0$.

2.1 Hyperplane Overcrowding

For a low-rank classifier $\mathbf{W} \in \mathbb{R}^{n \times d}$ and $d \ll n$, we have a large number of hyperplanes finely slicing a lower dimensional feature space. The natural question is, *out of the 2^n label combinations \mathbf{y} , how many can such a classifier actually represent?* To elaborate on this, let us define the set of argmaxable label combinations for a classifier \mathbf{W} as:

$$\mathcal{A}(\mathbf{W}) = \{\text{sign}(\mathbf{W}\mathbf{x}) \quad \forall \mathbf{x} \in \mathbb{R}^d\} \quad (1)$$

We can exactly count the number of argmaxable label combinations, i.e. $|\mathcal{A}(\mathbf{W})|$ if \mathbf{W} is in **general position**.

Definition 2. $\mathbf{W} \in \mathbb{R}^{n \times d}$ is in **general position** if no subset of d rows is linearly dependent. See Appendix A.

Theorem 1. (Cover 1965, Thm 2) If \mathbf{W} is in general position, the number of argmaxable label combinations is:

$$|\mathcal{A}(\mathbf{W})| = 2 \sum_{d'=0}^{d-1} \binom{n-1}{d'}. \quad (2)$$

It follows that i) the number of argmaxable label combinations depends only on n and d , not the specific \mathbf{W} , and ii) most label combinations will be unargmaxable for $d \ll n$ as Eq. (2) indicates an exponential growth (see Fig. 2).

While we can count the number of (un)argmaxable label combinations, it remains an open problem to verify if a specific set of label combinations can ever be predicted by a given classifier. We provide a solution in the next section.

3 Verifying Argmaxable Label Assignments

Given a low-rank classifier \mathbf{W} , we are interested in verifying if a set of L label combinations of interest $\{\mathbf{y}^{(j)}\}_{j=1}^L$ is (un)argmaxable. These labels can belong to a held out set, as in our experiments (Section 5), and help quantify the generalizability and trustworthiness of the given classifier, as we would expect it to be able to predict all L outputs.

A simple strategy is to verify the argmaxability of each $\mathbf{y}^{(j)}$. For that, we use a Chebyshev Linear Programme (LP), which also gives us a proxy for the size of a region, as we explain next. The LP aims to find the Chebyshev center (Boyd and Vandenberghe 2004, p. 417) of the region encoded by $\mathbf{y}^{(j)}$: the center of the largest ball of radius ϵ that can be embedded within it (see Fig. 3). As a constrained optimization problem, we want to solve:

$$\begin{aligned} & \text{maximise} \quad \epsilon \\ & \text{subject to} \quad \mathbf{w}_i^\top \mathbf{x} + \epsilon \|\mathbf{w}_i\|_2 \leq 0, \quad 1 \leq i \leq n, \\ & \quad -10^4 \leq \mathbf{x}_j \leq 10^4, \quad 1 \leq j \leq d, \quad \epsilon > \text{eps} \end{aligned} \quad (3)$$

where we constrain each entry of \mathbf{x} in a bounded region, since the Chebyshev center is not defined otherwise. If the LP is feasible it returns the maximum radius ϵ and we verify that \mathbf{y} is argmaxable. Note that we add an additional constraint, $\epsilon > \text{eps}$, where eps is the numerical accuracy that an LP solver can operate with.⁴ This tells us that while argmaxability can be defined in absolute terms, in practice it can only be verified up to some numerical precision: \mathbf{y} can be

⁴We use Gurobi Optimization (2021) which has $\text{eps}=10^{-8}$.

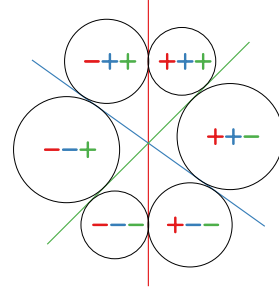


Figure 3: Our example from Figure 1 with $n=3$ and $d=2$. We include the balls found by the Chebyshev LP for each argmaxable label combination. When we have a narrow sigmoid bottleneck, most balls will have a tiny radius.

argmaxable as per Section 2, but an LP might not be able to detect it if there is only a tiny neighbourhood around a certain embedding \mathbf{x} . As such, we define ϵ -argmaxability to characterise robustly argmaxable label combinations.

Definition 3. A label assignment \mathbf{y} is **ϵ -argmaxable** for a classifier \mathbf{W} if it is argmaxable even under the presence of a noise vector δ having magnitude $\|\delta\|_2 \leq \epsilon$:

$$\mathbf{y} \text{ is } \epsilon\text{-argmaxable} \iff \exists \mathbf{x} : \text{sign}(\mathbf{W}(\mathbf{x} + \delta)) = \mathbf{y}.$$

Our Chebyshev LP is able to verify ϵ -argmaxability and therefore argmaxability, as the first implies the second. Note, however, that the reverse is not true. While verifying that a classifier is able to argmax a certain set of labels is of extreme importance, verification can be computationally expensive, as LPs become intractable as we scale n , d and L . To avoid this, we devise a classifier that guarantees that all labels of interest are argmaxable *by design*.

4 DFT Layers for k -Active MLC

Designing a low-rank BSL that guarantees argmaxability for all 2^n possible label combinations is impossible, according to Theorem 1. However, for most MLC datasets the label combinations are *sparse*; only a handful of labels are *active* for any given example. As such, herein we choose an upper bound k on the number of active labels for each dataset and show how to modify the parametrisation of a BSL so that any k -active label assignment is guaranteed to be argmaxable. We first define sufficient criteria by specifying a *broad family of parametrisations* for which our result holds: the weight matrix should have at least $2k + 1$ input features and all its maximal minors should be non-zero and have the same sign. Next, we *specify* an implementation satisfying these criteria, the Discrete Fourier Transform (DFT) layer, which is computationally appealing and is accurate in practice.

4.1 k -Active Label Assignments

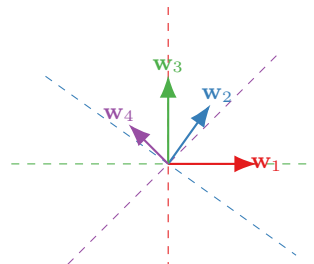
Label combinations in real-world MLC datasets are often sparse (Babbar and Schölkopf 2019); it is unlikely an image will contain more than k objects or that a clinical document will be assigned more than k clinical codes, where $k \approx \mathcal{O}(\log n)$ is a dataset dependent upper bound on the number of active labels. We now show how to guarantee that all k -active outputs are argmaxable by controlling the parametrisation of a BSL. We first formalize what a k -active label combination is below.

Figure 4: Visual evidence of Theorem 3. a) We construct a BSL having $n = 4$ labels and $d = 2$ features parametrised by $\mathbf{W} \in \mathbb{R}^{4 \times 2}$ such that all maximal minors are positive, i.e. $\mathbf{W} \in Gr_{n=4, d=2}^+$. (b) The rows of the matrix are binary classifiers, we demarcate the decision boundaries for each classifier using a dashed line. (c) We assign each region a sign vector corresponding to which labels the BSL would flag as active for an input falling in that region. As per Theorem 3, exactly the $(d-1) = 1$ -alternating outputs are argmaxable. More generally, for $d = 2k+1$, all k -active outputs are argmaxable (see Appendix K).

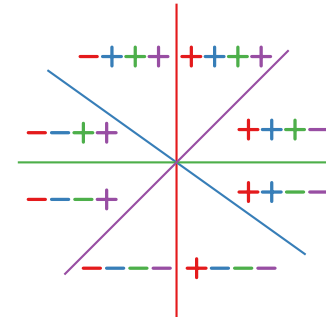
$$\mathbf{W} = \begin{bmatrix} 1.0 & 0.0 \\ 0.5 & 0.7 \\ 0.0 & 1.0 \\ -0.5 & 0.5 \end{bmatrix}$$

$$\begin{aligned} \Delta_{\{1,2\}} &= .7 & \Delta_{\{2,3\}} &= .5 \\ \Delta_{\{1,3\}} &= 1. & \Delta_{\{2,4\}} &= .6 \\ \Delta_{\{1,4\}} &= .5 & \Delta_{\{3,4\}} &= .5 \end{aligned}$$

(a) All $\binom{4}{2} = 6$ maximal minors, Δ_I , are positive, hence $\mathbf{W} \in Gr_{4,2}^+$.



(b) Correspondence of \mathbf{W} and geometric picture: each normal vector is a row of \mathbf{W} .



(c) The Argmaxable label assignments are the 1-alternating vectors, $\mathcal{A}(\mathbf{W}) = V_{4,1}$.

Definition 4. For a label assignment \mathbf{y} we define $\text{act}(\mathbf{y})$ to be the number of active labels in \mathbf{y} , i.e.:

$$\text{act}(\mathbf{y}) = \sum_{i=1}^n \mathbf{1}_{\mathbf{y}} \{y_i = +\}, \quad i \in [n] \quad (4)$$

e.g. $\text{act}(- - - -) = 0$ and $\text{act}(+ - - + -) = 2$.

Definition 5. The set of k -active label combinations on n labels is:

$$A_{n,k} = \{\mathbf{y} : \text{act}(\mathbf{y}) \leq k\} \quad (5)$$

For example, the MIMIC-III dataset (Johnson et al. 2016; Mullenbach et al. 2018) has $n = 8921$ labels, but no example has more than 80 active labels. Next we show how to guarantee that all labels in $A_{8921,80}$ are argmaxable.

4.2 k -Active Argmaxability Guarantees

Our goal in this section is to prove Theorem 4, which states that a *general criterion* for guaranteeing all k -active labels are argmaxable is that the weight matrix $\mathbf{W} \in \mathbb{R}^{n \times d}$, $d \geq 2k+1$ that parametrises the BSL has *maximal minors that agree in sign and are non-zero*. As such, we next introduce maximal minors and the family of matrices with the above property. We prove our result by showing that the argmaxable label assignments for this family of matrices are “ $2k$ -alternating” and that these subsume the k -active ones.

A **maximal minor** Δ_I of a $n \times d$ matrix, $n > d$, is the determinant of any $d \times d$ submatrix formed by selecting any d rows (indexed by I), without permuting them. For example, in Fig. 4a, all maximal minors are positive. We denote with $Gr_{n,d}^+$ the set of all matrices $\mathbf{W} \in \mathbb{R}^{n \times d}$ whose maximal minors are non-zero and have the same sign (see Appendix C). To prove Theorem 4, we build on facts known about k -alternating outputs, which we introduce below.

Definition 6. For a label assignment \mathbf{y} we define $\text{alt}(\mathbf{y})$ to be the number of sign changes encountered when reading the sequence of labels from left to right, i.e.:

$$\text{alt}(\mathbf{y}) = \sum_{i=1}^n \mathbf{1}_{\mathbf{y}} \{y_i \neq y_{i+1}\}, \quad i \in [n-1] \quad (6)$$

e.g. $\text{alt}(+ + - - -) = 1$ and $\text{alt}(+ + - + -) = 3$.

Definition 7. The set of k -alternating label assignments is:

$$V_{n,k} = \{\mathbf{y} : \text{alt}(\mathbf{y}) \leq k\} \quad (7)$$

Lemma 1. \mathbf{y} is k -active $\implies \mathbf{y}$ is at most $2k$ -alternating.

See Appendix D.1 for reasoning.

Theorem 2. (Gantmakher and Krein 1961) see (Karp 2017, Theorem 1.1). If all maximal minors of $\mathbf{W} \in \mathbb{R}^{n \times d}$ are non-zero and have the same sign, all label assignments \mathbf{y} computed as $\mathbf{y} = \text{sign}(\mathbf{W}\mathbf{x})$, $\mathbf{x} \in \mathbb{R}^d$ are at most $d-1$ alternating. $\mathbf{W} \in Gr_{n,d}^+ \implies \text{alt}(\mathbf{y}) \leq d-1$.

Theorem 3. For $\mathbf{W} \in Gr_{n,d}^+$ the argmaxable label assignments are exactly the $(d-1)$ -alternating vectors. $\mathbf{W} \in Gr_{n,d}^+ \implies \mathcal{A}(\mathbf{W}) = V_{n,d-1}$.

See Appendix D.2 for a proof and Fig. 4 for intuition.

Theorem 4. Consider a BSL parametrised by $\mathbf{W} \in Gr_{n,2k+1}^+$ which predicts label assignments using argmax prediction, $\mathbf{y} = \text{sign}(\mathbf{W}\mathbf{x})$. All k -active label assignments are argmaxable: $A_{n,k} \subset \mathcal{A}(\mathbf{W})$.

Proof. From Theorem 3, for \mathbf{W} in $Gr_{n,2k+1}^+$ the set of $2k$ -alternating label assignments $V_{n,2k}$ is argmaxable. Then, from Lemma 1, we have $A_{n,k} \subseteq V_{n,2k} = \mathcal{A}(\mathbf{W})$, and therefore all k -active labels are argmaxable. \square

In summary, we showed that if $\mathbf{W} \in Gr_{n,2k+1}^+$, all k -active outputs are argmaxable, but we have not given a concrete implementation. We next introduce the DFT layer, a practical and efficient member of the $Gr_{n,2k+1}^+$ family.

4.3 DFT Layers

Herein we engineer a specific BSL parametrisation that satisfies Theorem 4 and relies on the Discrete Fourier Transform (DFT). In addition to this property, the DFT is appealing also because: a) it allows to reduce the number

of learnable parameters as the DFT coefficients can be fixed⁵ and b) we can compute the activation of the DFT Layer in $\mathcal{O}(n \log n)$ time via the Fast Fourier Transform (see Appendix E) instead of a more expensive $\mathcal{O}(n^2)$ generic matrix-vector product. We next describe a truncated DFT matrix and show that it provides the guarantees we seek. For the DFT matrix, we truncate frequencies larger than k :

$$\mathbf{W}_{n,2k+1}^{\text{DFT}} = \begin{bmatrix} \frac{1}{\sqrt{n}} & \sqrt{\frac{2}{n}} \cos t_1 & \sqrt{\frac{2}{n}} \sin t_1 & \cdots & \sqrt{\frac{2}{n}} \cos kt_1 & \sqrt{\frac{2}{n}} \sin kt_1 \\ \frac{1}{\sqrt{n}} & \sqrt{\frac{2}{n}} \cos t_2 & \sqrt{\frac{2}{n}} \sin t_2 & \cdots & \sqrt{\frac{2}{n}} \cos kt_2 & \sqrt{\frac{2}{n}} \sin kt_2 \\ \vdots & \vdots & \vdots & \ddots & \vdots & \vdots \\ \frac{1}{\sqrt{n}} & \sqrt{\frac{2}{n}} \cos t_n & \sqrt{\frac{2}{n}} \sin t_n & \cdots & \sqrt{\frac{2}{n}} \cos kt_n & \sqrt{\frac{2}{n}} \sin kt_n \end{bmatrix},$$

$$t_i = \frac{2\pi(i-1)}{n}, i \in [n] \quad (8)$$

Lemma 2. A truncated DFT matrix $\mathbf{W}_{n,2k+1}^{\text{DFT}} \in Gr_{n,2k+1}^+$.

We need to show that the maximal minors of $\mathbf{W}_{n,2k+1}^{\text{DFT}}$ are non-zero and agree in sign. See Appendix D.3 for a proof.

Problem: Regions can become too small. While in practice we could use the fixed DFT Layer as defined above and rely on an expressive feature encoder to do the heavy lifting, if the number of labels n is much greater than the number of features $2k+1$, it becomes hard to classify some label assignments with large confidence. This is because segmenting a low dimensional space with very many hyperplanes induces regions that become arbitrarily small shards. In argmaxability terms, if we fix an ϵ and increase the number of labels, all k -active labels are argmaxable but increasingly more are not ϵ -argmaxable, see left in Fig. 5. This is a problem for any classifier \mathbf{W} , because for training and for generalisation we need to project points into large enough regions. However, we found that DFT layers are more susceptible to it (Appendix F.2) than general BSL (see Appendix I for a more rigorous explanation).

Solution: Slack variables. A practical way to deal with small regions is to increase the dimensionality of the feature vectors, by adding *slack variables*, see bottom of Fig. 5. Importantly, as we show next in Lemma 3, we can do so while retaining our guarantees.

Lemma 3. Assume a label \mathbf{y} is argmaxable for a classifier $\mathbf{W} \in \mathbb{R}^{n \times d}$. Consider increasing the dimensionality of the features of the classifier \mathbf{W} by adding s more randomly initialised slack columns $\mathbf{S} \in \mathbb{R}^{n \times s}$. The label \mathbf{y} is also argmaxable in $\mathbf{W}' = [\mathbf{W} \ \mathbf{S}]$, $\mathbf{W}' \in \mathbb{R}^{n \times (d+s)}$.

Proof. Consider the input feature vector for \mathbf{W}' , $\mathbf{x}' = \begin{bmatrix} \mathbf{x} \\ \mathbf{x}_s \end{bmatrix}$, $\mathbf{x} \in \mathbb{R}^d$, $\mathbf{x}_s \in \mathbb{R}^s$. Set $\mathbf{x}_s = \mathbf{0}$. Then notice that

$\mathbf{y} = \text{sign} \left([\mathbf{W} \ \mathbf{S}] \begin{bmatrix} \mathbf{x} \\ \mathbf{0} \end{bmatrix} \right) = \text{sign}(\mathbf{W}\mathbf{x})$ is equivalent to the original classifier, so if \mathbf{y} is argmaxable in \mathbf{W} it is also argmaxable in \mathbf{W}' by setting \mathbf{x}_s to zero. \square

As such, we propose the DFT layer, which has $(2k+1) \times n$ fixed parameters which enforce argmaxability and $s \times n$ learnable parameters which give it flexibility.

⁵In early experiments we parametrised and learned the t_i of the DFT matrix but found little impact on the results.

ϵ -Argmaxability of k -Active Label Assignments

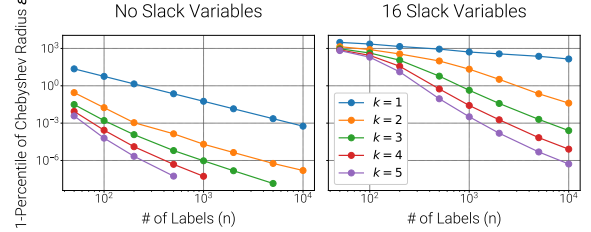


Figure 5: **Left:** As we increase the number of labels n for the DFT Layer, the radii of the regions shrink, making them harder to predict in practice. **Right:** Adding slack variables ameliorates this problem. We plot ϵ -argmaxability (Definition 3), measured here for the 1% of labels that have radius less than that plotted. For the DFT Layer, i.e. $\mathbf{W} = \mathbf{W}_{n,2k+1}^{\text{DFT}}$, all k -active label assignments are argmaxable, but as we increase n , some ($k \geq 3$) cannot be detected at the precision of the LP (10^{-8}). Adding 16 randomly initialised slack columns, i.e. $\mathbf{W} = [\mathbf{W}_{n,2k+1}^{\text{DFT}} \ \mathbf{S}]$, makes the regions ϵ -argmaxable with larger ϵ .

5 Experiments

We now empirically evaluate the BSL and DFT layers on three MLC datasets and answer the following research questions: **RQ1)** Do BSLs have unargmaxable labels in practice? **RQ2)** Can DFT layers guarantee that meaningful labels are argmaxable in practice? **RQ3)** What is the trade-off between performance and the number of trainable parameters? We answer the above after introducing the models and datasets.

5.1 Model Setup

We define the two MLC output layers we will compare, the *BSL Layer* that is unconstrained and does not guarantee argmaxability of k active outputs, and our *DFT layer* which does. In our experiments we want to study the effect of varying the bottleneck width, d , irrespective of the feature dimensionality of the encoder which varies across datasets and models. We therefore introduce an *affine projection layer* (parametrised by \mathbf{P} and \mathbf{b}) between the feature encoder and the *linear classifier* (parametrised by \mathbf{W}). For simplicity, we do not include bias terms for the classifiers. For both models, we compute the logits $\mathbf{z} \in \mathbb{R}^n$ from the encoder activation $\mathbf{e} \in \mathbb{R}^e$ as:

$$\mathbf{z} = \mathbf{W}\mathbf{e}, \quad \mathbf{x} = \mathbf{Pe} + \mathbf{b} \quad (9)$$

but the parametrisations differ, as we discuss next.

BSL Output Layer For the BSL, the projection layer maps from e , the dimensionality of the encoder embeddings, to d , the feature dimensionality using $\mathbf{P} \in \mathbb{R}^{e \times d}$ and bias $\mathbf{b} \in \mathbb{R}^d$. This is followed by the linear classifier $\mathbf{W} \in \mathbb{R}^{n \times d}$.

DFT Output Layer For the DFT, we first pick the maximum number of active labels, k , depending on the statistics of the dataset. We then set the number of slack dimensions to be d so we can directly compare to the BSL.

For the DFT, we have $\mathbf{P} \in \mathbb{R}^{e \times (2k+1+d)}$ and $\mathbf{b} \in \mathbb{R}^{(2k+1+d)}$ since we include $2k+1$ more features that map to the DFT columns of the classifier. The learnable parameters of the classifier comprise d slack columns. Conceptually, and for the purposes of checking the classifier with our LP, we construct the classifier by concatenating the fixed DFT matrix to the slack columns, i.e. $\mathbf{W} = [\mathbf{W}_{n,2k+1}^{\text{DFT}} \ \mathbf{S}]$, $\mathbf{W} \in \mathbb{R}^{n \times (2k+1+d)}$. In practice we compute the logits \mathbf{z} efficiently as $\mathbf{z} = \text{FFT}(\mathbf{x}_{:2k+1}) + \mathbf{S}\mathbf{x}_{2k+1:}$ (see Appendix E).

Initialisation Trick For the DFT, we can speed up training by exploiting the fact that a) we know \mathbf{W}^{DFT} and it is fixed and b) we know that outputs are k -active. The key insight is that due to the outputs being k -active, we would prefer to assign a probability $\frac{k}{n}$ to all labels when we start training. To achieve this, we can exploit the fact that the first column of \mathbf{W}^{DFT} is $\frac{1}{\sqrt{n}}$ and initialise the bias vector of the projection layer to be $[\sqrt{n} \log(\frac{k}{n}), 0, \dots, 0]$, where the logit function is the inverse of sigmoid. This way, assuming logits are close to zero when we begin training, the model will assign probability approximately $\frac{k}{n}$ to each label instead of $\frac{1}{2}$. A similar bias initialisation idea for MLC was discussed in (Schultheis and Babbar 2022), but it was not used in a neural network.

Computational Cost of DFT Compared to the BSL, the cost of the DFT layer with n labels is a cheap $\mathcal{O}(n \log n)$ matrix vector multiplication and an increase in trainable parameters in the projection layer.

While the DFT has $e \times (2k+1)$ more trainable parameters in the projection layer than a BSL, as we will see in our results, it can have a much lower trainable parameter count overall because it is more parameter efficient to allocate more parameters in the projection layer than the classifier. To elaborate, the MIMIC-III CNN models (Mullenbach et al. 2018) have $n = 8921$ and $e = 500$, which means that the number of trainable parameters grows 9 times more if we increase d compared to increasing k . More precisely, for $k = 80$, the number of added parameters in the projection layer is 161×500 , which we can match by decreasing d in the output layer of a BSL by only 9.

5.2 MLC Tasks (Datasets)

We next introduce the three datasets and summarise important attributes in Table 1, see Appendix H for detailed dataset construction and Appendix H.2 for more dataset statistics.

Table 1: Setup: Number of labels, n , max number of active labels, k , and number of training examples, N .

MLC Dataset	n	k	N	encoder	modality
MIMIC-III	8921	80	44k	CNN (e=500)	text
BioASQ task A	20000	50	100k	PubMedBERT (e=768)	text
OpenImagesV6	8933	50	108k	TResnet (e=2432)	images

Clinical Coding (MIMIC-III) We first test the DFT layer on MIMIC-III (Johnson et al. 2016). For this safety critical application of clinical coding, the goal is to tag each clinical note with a set of relevant ICD-9 codes which describe

findings (see Fig. 1). We retrain the CNN encoder model defined in Mullenbach et al. (2018) which has $n = 8921$ and $e = 500$. We use the same word embeddings, preprocessed data, data splits, metrics (Prec@8) and hyperparameters reported in the paper (Mullenbach et al. 2018), we only change the learning rate of the Adam optimiser to 0.001, as this improves results (as also found by Edin et al. (2023)).

Semantic Indexing (BioASQ Task A) We next turn to MLC on the 2021 BioASQ semantic indexing challenge (Tsatsaronis et al. 2015; Nentidis et al. 2021; Krithara et al. 2023). For this task, we are given PubMed abstracts and asked to predict a set of relevant MeSH headings⁶ for each article. We create dataset splits (see Appendix H.2 for details) which cover $n = 20000$ labels, making sure that all individual labels occur in both the train and test sets. We do so to avoid claiming a label assignment is unargmaxable when in fact it would be impossible to predict the labels that constitute it. We use $k = 50$ since this is by construction the maximum number of active labels per example for this dataset. We finetune PubMedBERT (Gu et al. 2021), a domain specific uncased BERT (Devlin et al. 2019) encoder that has $e = 768$ and has been pretrained on PubMed abstracts. We use early stopping with a patience of 10 on the validation crossentropy loss.

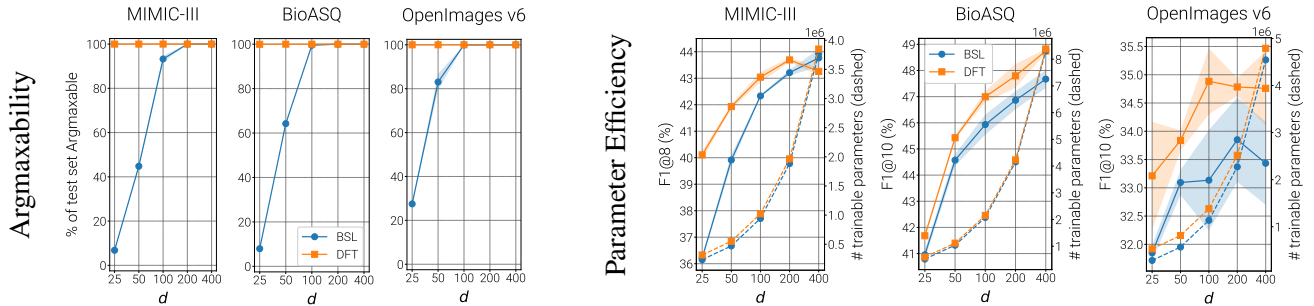
Image MLC (OpenImages v6) We use the OpenImages v6 dataset (Kuznetsova et al. 2020)⁷ where the goal is to tag each image with objects that appear in it. Similar to the BioASQ case, we choose the label vocabulary $n = 8933$ such that all examples in the train, validation and test set are covered. We pick $k = 50$ since the training data has at most 45 active labels per example. We finetune the TResnet (Ridnik et al. 2020) with $e = 2432$ that Baruch et al. (2020) pretrained for MLC on this dataset. We use early stopping with a patience of 10 on the validation crossentropy loss.

5.3 Results

RQ1) BSL: Unargmaxable outputs We use the LP to verify the BSL on the test sets. As can be seen in Fig. 6a, for $d > 200$ all the examples in the test set are argmaxable for the BSL. However, as we reduce d , the number of unargmaxable label assignments increases for all datasets. More specifically, we first get unargmaxable outputs at $d = 200$ for MIMIC-III (see Appendix F). Analogous considerations can be drawn for BioASQ and OpenImages (Fig. 6a). As such, we conclude that unargmaxability can indeed be an issue when d is not large enough. Note that one can never determine a d that can always guarantee all label configurations of interest to be argmaxable: even an exhaustive verification on all test samples does not imply that future unseen configurations will be argmaxable. **RQ2) DFT: Argmaxability** While we know that the DFT layer guarantees argmaxability in theory, we also see that it works in practice (apart from a handful of outputs when $d = 25$, which are ϵ -unargmaxable, see Appendix F.2). Crucially, these guarantees also apply to

⁶<https://www.nlm.nih.gov/mesh/meshhome.html>

⁷https://storage.googleapis.com/openimages/web/download_v6.html



(a) Our DFT layer does not suffer from unargmaxable test examples. BSLs cannot provide any such guarantees.

(b) Our DFT layer is more parameter efficient. F1 is overall better than the BSL, so we can match BSL's F1 with fewer trainable parameters (smaller d).

Figure 6: Comparison of BSL and our DFT output layer on three MLC datasets. We vary, d , the number of trainable dimensions and plot the mean and std (shaded) over 3 runs with different random seeds. Left: We use the LP to verify the output layers on the test sets. When $d < 200$ a large percentage of label configurations becomes unargmaxable for the BSL, in contrast to our DFT. Right: Performance in F1@8 or F1@10 (left axis) in terms of the number of trainable parameters (right axis, dashed lines). Our DFT is better ($d \leq 200$) or comparable to the BSL (MIMIC-III, $d > 200$). We can therefore retain a high F1@k score for DFT even if we reduce the number of trainable parameters by making the bottleneck narrower. For example, on BioASQ we can surpass the F1@10 of the BSL that has $d = 200$ with a DFT of $d = 100$, which has about **50% fewer trainable parameters**.

unseen k -active label assignments; this would be impossible to enforce with BSLs, as discussed. **RQ3) Parameter Efficiency** In addition, we turn to Fig. 6b, and see that the DFT layer outperforms the BSL layer by a wide margin for small d . This allows us to match the performance of the BSL using a DFT with smaller d and hence fewer trainable parameters. As can be seen, in some cases DFT layers obtain better or comparable performance with up to 50% less trainable parameters. **Convergence speed** Lastly, DFT layers converge faster due to the initialisation trick, see Appendix G.

6 Related Work

Low-rank Parametrisations in MLC. Low-rank one-vs-all classifiers (Jain et al. 2019) are a common parametrisation in MLC due to their simplicity. Previous work has highlighted that low-rank parametrisations can be problematic (Bhatia et al. 2015; Xu, Tao, and Xu 2016; Tagami 2017), but the argument has been from a matrix factorisation perspective, e.g. that low-rank factorisations reconstruct the label matrix with high error when there are long-tail labels. Herein, we highlight a more tangible limitation of low-rank parametrisations for bottlenecked classifiers: meaningful label assignments can be unargmaxable. While we prove that we can retain argmaxability with a very low-rank matrix, we agree that low-rank parametrisations can still be problematic, since the matrix must be higher rank in order to retain ϵ -argmaxability which is needed in practice both for training and prediction.

Graph Embeddings in Euclidean Space. Our work is also connected to whether a graph can be embedded in Euclidean space. Alon, Moran, and Yehudayoff (2015) study the rank of sets of sign vectors and whether they can be embedded in d dimensions. In a similar vein to our theoretical results for k -active MLC, Chanpuriya et al. (2020) use a Vandermonde construction to prove the existence of a factorisable adjacency matrix for any graph of bounded degree k . Vandermonde matrices also satisfy the criteria we pre-

sented in Section 4.2, bridging our more general result with theirs may be an interesting direction.

7 Discussion and Conclusion

Through extensive experiments on three multi-label classification datasets we have shown that bottlenecked multi-label classifiers – which are still ubiquitous in large MLC scenarios (Mullenbach et al. 2018; Baruch et al. 2020) – can have unargmaxable label assignments when the label vocabulary is much larger than the dimensionality of the input features (Section 5). We believe practitioners should at the very least be aware that selecting the feature dimension of a BSL is not an innocuous hyperparameter search: by lowering the rank of the output layer they are potentially making some label assignments impossible to predict. Unargmaxability impacts the generalization and trustworthiness of these classifiers since BSLs cannot guarantee that meaningful label assignments will not be missed at test time or that the classifiers will not be targeted by adversarial attacks (Zhu et al. 2019; Aghakhani et al. 2021).

However, we showed that this does *not* have to be the case. We provided a family of parametrisations that guarantee that all label assignments having up to k active labels are argmaxable (Section 4.2) and implemented our DFT output layer which converges faster than a BSL, is up to 50% more parameter efficient, and outperforms or matches the BSL on three widely used MLC datasets. At the same time, our findings prompt several avenues for future work. For example, it is an open question whether there are more efficient or more expressive parametrisations that satisfy the criteria we outlined in Section 4.2. Additionally, as we make the Sigmoid Bottleneck narrower, labels get assigned to smaller and smaller regions that are harder to predict, and harder to verify (Section 3). This highlights an important research direction: parametrise output layers in a way that guarantees ϵ -argmaxability for large values of ϵ .

Acknowledgements

We would like to thank Lorenzo Loconte, Rickey Liang, Emile van Krieken and Marina Potsi for feedback on early drafts. Furthermore, Asif Khan for many discussions and help connecting the Cyclic Polytope to truncated DFT, Jesse Sigal for discussions on cyclic permutations, Matúš Falis for discussing multi-label classification and datasets, Tom Sherbourne for discussing DFT and low-pass filters and Ivan Titov and Henry Gouk for helpful suggestions and advice.

AG was supported by the Engineering and Physical Sciences Research Council (EP/R513209/1). AV was supported by the ‘‘UNREAL: Unified Reasoning Layer for Trustworthy ML’’ project (EP/Y023838/1) selected by the ERC and funded by UKRI EPSRC.

References

Aghakhani, H.; Meng, D.; Wang, Y.-X.; Kruegel, C.; and Vigna, G. 2021. Bullseye polytope: A scalable clean-label poisoning attack with improved transferability. In *2021 IEEE European Symposium on Security and Privacy (EuroS&P)*, 159–178. IEEE.

Alon, N.; Moran, S.; and Yehudayoff, A. 2015. Sign rank versus VC dimension. In *Annual Conference Computational Learning Theory*.

Babbar, R.; and Schölkopf, B. 2019. Data scarcity, robustness and extreme multi-label classification. *Machine Learning*, 1–23.

Baruch, E. B.; Ridnik, T.; Zamir, N.; Noy, A.; Friedman, I.; Protter, M.; and Zelnik-Manor, L. 2020. Asymmetric Loss For Multi-Label Classification. *2021 IEEE/CVF International Conference on Computer Vision (ICCV)*, 82–91.

Bhatia, K.; Jain, H.; Kar, P.; Varma, M.; and Jain, P. 2015. Sparse Local Embeddings for Extreme Multi-label Classification. In Cortes, C.; Lawrence, N.; Lee, D.; Sugiyama, M.; and Garnett, R., eds., *Advances in Neural Information Processing Systems*, volume 28. Curran Associates, Inc.

Björner, A.; Las Vergnas, M.; Sturmfels, B.; White, N.; and Ziegler, G. M. 1999. *Oriented Matroids*. Encyclopedia of Mathematics and its Applications. Cambridge University Press, 2 edition.

Boyd, S. P.; and Vandenberghe, L. 2004. *Convex optimization*. Cambridge University Press.

Chandramouli, S.; Musco, C.; Sotiroopoulos, K.; and Tsourakakis, C. 2020. Node Embeddings and Exact Low-Rank Representations of Complex Networks. In Larochelle, H.; Ranzato, M.; Hadsell, R.; Balcan, M.; and Lin, H., eds., *Advances in Neural Information Processing Systems*, volume 33, 13185–13198. Curran Associates, Inc.

Choi, E.; Levy, O.; Choi, Y.; and Zettlemoyer, L. 2018. Ultra-Fine Entity Typing. In *Proceedings of the 56th Annual Meeting of the Association for Computational Linguistics (Volume 1: Long Papers)*, 87–96. Melbourne, Australia: Association for Computational Linguistics.

Cordovil, R.; and Duchet, P. 2000. Cyclic Polytopes and Oriented Matroids. *Eur. J. Comb.*, 21: 49–64.

Cover, T. M. 1965. Geometrical and Statistical Properties of Systems of Linear Inequalities with Applications in Pattern Recognition. *IEEE Trans. Electron. Comput.*, 14: 326–334.

Demeter, D.; Kimmel, G.; and Downey, D. 2020. Stolen Probability: A Structural Weakness of Neural Language Models. In *Proceedings of the 58th Annual Meeting of the Association for Computational Linguistics*, 2191–2197. Online: Association for Computational Linguistics.

Devlin, J.; Chang, M.-W.; Lee, K.; and Toutanova, K. 2019. BERT: Pre-training of Deep Bidirectional Transformers for Language Understanding. In *Proceedings of the 2019 Conference of the North American Chapter of the Association for Computational Linguistics: Human Language Technologies, Volume 1 (Long and Short Papers)*, 4171–4186. Minneapolis, Minnesota: Association for Computational Linguistics.

Edin, J.; Junge, A.; Havtorn, J. D.; Borgholt, L.; Maistro, M.; Ruotsalo, T.; and Maaløe, L. 2023. Automated Medical Coding on MIMIC-III and MIMIC-IV: A Critical Review and Replicability Study. *Proceedings of the 46th International ACM SIGIR Conference on Research and Development in Information Retrieval*.

Gale, D. 1963. Neighborly and cyclic polytopes. In *Proceedings of Symposia in Pure Mathematics*, volume 7, 225–232.

Ganea, O.; Gelly, S.; Bécigneul, G.; and Severyn, A. 2019. Breaking the Softmax Bottleneck via Learnable Monotonic Pointwise Non-linearities. In *ICML*, 2073–2082.

Gantmakher, F.; and Krein, M. 1961. *Oscillation Matrices and Kernels and Small Vibrations of Mechanical Systems*. AMS/Chelsea Publication Series. USAEC Office of Technical Information. ISBN 9780821882412.

Grivas, A.; Bogoychev, N.; and Lopez, A. 2022. Low-Rank Softmax Can Have Unargmaxable Classes in Theory but Rarely in Practice. In *Proceedings of the 60th Annual Meeting of the Association for Computational Linguistics (Volume 1: Long Papers)*, 6738–6758. Dublin, Ireland: Association for Computational Linguistics.

Gu, Y.; Tinn, R.; Cheng, H.; Lucas, M.; Usuyama, N.; Liu, X.; Naumann, T.; Gao, J.; and Poon, H. 2021. Domain-Specific Language Model Pretraining for Biomedical Natural Language Processing. *ACM Trans. Comput. Healthcare*, 3(1).

Gurobi Optimization. 2021. Gurobi Optimizer Reference Manual.

Jain, H.; Balasubramanian, V.; Chunduri, B.; and Varma, M. 2019. Slice: Scalable Linear Extreme Classifiers Trained on 100 Million Labels for Related Searches. *Proceedings of the Twelfth ACM International Conference on Web Search and Data Mining*.

Järvelin, K.; and Kekäläinen, J. 2002. Cumulated gain-based evaluation of IR techniques. *ACM Trans. Inf. Syst.*, 20: 422–446.

Johnson, A. E. W.; Pollard, T. J.; Shen, L.; Lehman, L.-W. H.; Feng, M.; Ghassemi, M.; Moody, B.; Szolovits, P.; Celi, L. A.; and Mark, R. G. 2016. MIMIC-III, a freely accessible critical care database. *Sci. Data*, 3(1): 160035.

Karp, S. N. 2017. Sign variation, the Grassmannian, and total positivity. *Journal of Combinatorial Theory, Series A*, 145: 308–339.

Krithara, A.; Mork, J. G.; Nentidis, A.; and Paliouras, G. 2023. The road from manual to automatic semantic indexing of biomedical literature: a 10 years journey. *Frontiers in Research Metrics and Analytics*, 8.

Kulmanov, M.; and Hoehndorf, R. 2019. DeepGOPlus: improved protein function prediction from sequence. *Bioinformatics*, 36: 422–429.

Kuznetsova, A.; Rom, H.; Alldrin, N.; Uijlings, J.; Krasin, I.; Pont-Tuset, J.; Kamali, S.; Popov, S.; Malloci, M.; Kolesnikov, A.; Duerig, T.; and Ferrari, V. 2020. The Open Images Dataset V4: Unified image classification, object detection, and visual relationship detection at scale. *IJCV*.

Mullenbach, J.; Wiegreffe, S.; Duke, J. D.; Sun, J.; and Eisenstein, J. 2018. Explainable Prediction of Medical Codes from Clinical Text. In *NAACL*.

Nentidis, A.; Katsimpras, G.; Vandorou, E.; Krithara, A.; and Paliouras, G. 2021. Overview of BioASQ Tasks 9a, 9b and Synergy in CLEF2021. In *Conference and Labs of the Evaluation Forum*.

Paul, S.; and Rakshit, S. 2014. Large-scale multi-label text classification. [Online; accessed 15-August-2023].

Pedregosa, F.; Varoquaux, G.; Gramfort, A.; Michel, V.; Thirion, B.; Grisel, O.; Blondel, M.; Prettenhofer, P.; Weiss, R.; Dubourg, V.; Vanderplas, J.; Passos, A.; Cournapeau, D.; Brucher, M.; Perrot, M.; and Duchesnay, E. 2011. Scikit-learn: Machine Learning in Python. *Journal of Machine Learning Research*, 12: 2825–2830.

Postnikov, A. 2006. Total positivity, Grassmannians, and networks. *arXiv: Combinatorics*.

Ridnik, T.; Lawen, H.; Noy, A.; and Friedman, I. 2020. TResNet: High Performance GPU-Dedicated Architecture. *2021 IEEE Winter Conference on Applications of Computer Vision (WACV)*, 1399–1408.

Schultheis, E.; and Babbar, R. 2022. Speeding-up one-versus-all training for extreme classification via mean-separating initialization. *Machine Learning*, 111(11): 3953–3976.

Tagami, Y. 2017. AnnexML: Approximate Nearest Neighbor Search for Extreme Multi-label Classification. *Proceedings of the 23rd ACM SIGKDD International Conference on Knowledge Discovery and Data Mining*.

Tsatsaronis, G.; Balikas, G.; Malakasiotis, P.; Partalas, I.; Zschunke, M.; Alvers, M. R.; Weissenborn, D.; Krithara, A.; Petridis, S.; Polychronopoulos, D.; Almirantis, Y.; Pavlopoulos, J.; Baskiotis, N.; Gallinari, P.; Artières, T.; Ngomo, A.-C. N.; Heino, N.; Gaussier, É.; Barrio-Alvers, L.; Schroeder, M.; Androutsopoulos, I.; and Paliouras, G. 2015. An overview of the BIOASQ large-scale biomedical semantic indexing and question answering competition. *BMC Bioinformatics*, 16.

Xu, C.; Tao, D.; and Xu, C. 2016. Robust Extreme Multi-label Learning. *Proceedings of the 22nd ACM SIGKDD International Conference on Knowledge Discovery and Data Mining*.

Yang, Z.; Dai, Z.; Salakhutdinov, R.; and Cohen, W. W. 2018. Breaking the Softmax Bottleneck: A High-Rank RNN Language Model. In *6th International Conference on Learning Representations, ICLR 2018, Vancouver, BC, Canada, April 30 - May 3, 2018, Conference Track Proceedings*.

Zhu, C.; Huang, W. R.; Li, H.; Taylor, G.; Studer, C.; and Goldstein, T. 2019. Transferable clean-label poisoning attacks on deep neural nets. In *International Conference on Machine Learning*, 7614–7623. PMLR.

Ziegler, G. M. 1994. *Lectures on Polytopes*. Springer New York, NY.

A Points in General Position

Definition 8. We say n points are in **general position** in \mathbb{R}^d if any subset of d or fewer points is linearly independent.

Intuitively, this means that the points are no more dependent than they need to be in \mathbb{R}^d . No 2 points lie on a line through the origin, no 3 points lie on a plane through the origin, no d points lie in a $d - 1$ subspace. Algebraically, it means that a $d \times d$ matrix formed by stacking any d points together has non-zero determinant.

Definition 9. Consider n points in \mathbb{R}^d stacked in the rows of $\mathbf{W} \in \mathbb{R}^{n \times d}$. The points are **linearly dependent** if:

$$\exists \mathbf{z}, \mathbf{z} \neq \mathbf{0} : \mathbf{z}^\top \mathbf{W} = \mathbf{0} \quad (10)$$

B The Cyclic Polytope

To prove Lemma 2 in the next section, we leverage the theorem in Cordovil and Duchet (2000), who present their result in terms of the homogenisation of the Cyclic Polytope. Herein we highlight the equivalence of the homogenisation of the Cyclic Polytope to a DFT matrix with total order constraints on the t_i . We will need this to make claims about the maximal minors of the DFT matrix.

The Cyclic Polytope We start with the standard definition. The $\mathcal{C}_{n,d}$ with n vertices in \mathbb{R}^d is defined as the convex hull of $n > d$ distinct points on the moment curve in \mathbb{R}^d (Ziegler 1994, Example 0.6, p.11). The moment curve is a map $m(t) : \mathbb{R} \mapsto \mathbb{R}^d$ defined as:

$$\mathcal{C}_{n,d} = \text{conv} (m(t_1), m(t_2), \dots, m(t_n)) \quad (11)$$

$$\text{where } m(t) = \begin{bmatrix} t \\ t^2 \\ \vdots \\ t^d \end{bmatrix}, \quad t_1 < t_2 < \dots < t_n \quad (12)$$

Homogenisation We move from affine to linear space by appending an extra dimension and fixing it to 1, i.e. we have $\text{hom} : \mathbb{R}^d \rightarrow \mathbb{R}^{d+1}$, $\text{hom}(\mathbf{x}) = \begin{pmatrix} 1 \\ \mathbf{x} \end{pmatrix}$. To conform with earlier notation, we will stack the vertices of the Cyclic Polytope in the rows of the matrix. For the standard Cyclic Polytope on the moment curve we get a Vandermonde matrix:

$$\mathcal{C}_{n,d} = \begin{bmatrix} t_1 & t_1^2 & \dots & t_1^d \\ t_2 & t_2^2 & \dots & t_2^d \\ \vdots & \vdots & \ddots & \vdots \\ t_n & t_n^2 & \dots & t_n^d \end{bmatrix} \quad (13)$$

$$\text{hom}(\mathcal{C}_{n,d}) = \begin{bmatrix} 1 & t_1 & t_1^2 & \dots & t_1^d \\ 1 & t_2 & t_2^2 & \dots & t_2^d \\ \vdots & \vdots & \vdots & \ddots & \vdots \\ 1 & t_n & t_n^2 & \dots & t_n^d \end{bmatrix} \quad (14)$$

Trigonometric Cyclic Polytope Instead of the moment curve, Gale (1963) used the trigonometric moment curve to construct the Cyclic Polytope. We note that its homogenisation is the truncated DFT matrix.

$$\mathcal{C}_{n,2k} = \begin{bmatrix} \cos t_1 & \sin t_1 & \dots & \cos kt_1 & \sin kt_1 \\ \cos t_2 & \sin t_2 & \dots & \cos kt_2 & \sin kt_2 \\ \vdots & \vdots & \ddots & \vdots & \vdots \\ \cos t_n & \sin t_n & \dots & \cos kt_n & \sin kt_n \end{bmatrix} \quad (15)$$

$$\text{hom}(\mathcal{C}_{n,2k}) = \begin{bmatrix} 1 & \cos t_1 & \sin t_1 & \dots & \cos kt_1 & \sin kt_1 \\ 1 & \cos t_2 & \sin t_2 & \dots & \cos kt_2 & \sin kt_2 \\ \vdots & \vdots & \vdots & \ddots & \vdots & \vdots \\ 1 & \cos t_n & \sin t_n & \dots & \cos kt_n & \sin kt_n \end{bmatrix} \quad (16)$$

In Appendix D.3, we will use the connection between the DFT matrix and the Cyclic Polytope to prove Lemma 2.

C Grassmannians

The **Grassmannian** $Gr_{n,d}$ is the set of all d -dimensional subspaces of \mathbb{R}^n . We will think of $Gr_{n,d}$ as the space of rank d matrices $\mathbf{W} \in \mathbb{R}^{n \times d}$ with $1 \leq d \leq n$. More precisely, a single member of $Gr_{n,d}$ defines a subspace and corresponds to all \mathbf{W} that form a basis for that subspace, i.e. all matrices obtained by multiplying the basis on the right by any invertible $d \times d$ matrix.⁸ We can subdivide the whole Grassmannian into more granular matrix families by considering the sign of the maximal minors. For the scope of this paper, we are specially interested in the **Totally Positive Grassmannian** $Gr_{n,d}^+$, the space of $n \times d$ matrices for which all maximal minors are non-zero and have the same sign (see also Postnikov (2006, Definition 3.1)).

D Proofs

D.1 Lemma 1

\mathbf{y} is k -active $\implies \mathbf{y}$ is at most $2k$ -alternating.

Proof. Construct a k -active \mathbf{y} of length n from the all inactive \mathbf{y} by flipping all signs after any of the $n - 1$ positions between labels. We need at most $2k$ distinct flips, i.e. when the active labels are not adjacent and do not include the 1st or n^{th} label and less otherwise. For example, $-+--$ can be produced with 2 flips starting from the all inactive vector: $-+-- \rightarrow -++ \rightarrow -+-$. \square

D.2 Theorem 3

Proof. Since $\mathbf{W} \in Gr_{n,d}^+$, all maximal minors are non-zero and hence the rows of \mathbf{W} are in general position (see Definition 2). By invoking Theorem 1, the number of argmaxable label assignments is $|\mathcal{A}(\mathbf{W})| = 2 \sum_{d'=0}^{d-1} \binom{n-1}{d'}$. Note that this is exactly the number of $(d - 1)$ -alternating label assignments $|V_{n,d-1}|$ as we elaborate on next. The binomial coefficient comes from choosing d' out of the $n - 1$ positions between labels to flip the sign and we sum over all possible number of sign changes up to $d - 1$. For each alternating \mathbf{y} , we can produce another by flipping all signs, hence the leading multiplier 2. Now, from Theorem 2, none of the label assignments can have more than $d - 1$ sign changes;

⁸Column operations change the basis of the columnspace but not the subspace itself.

hence they must be exactly the $(d - 1)$ -alternating label assignments: $\mathcal{A}(\mathbf{W}) = V_{n,d-1}$. \square

D.3 Lemma 2

Proof. The DFT matrix corresponds to the homogenisation of the vertices of a Cyclic Polytope (Gale 1963; Cordovil and Duchet 2000), see Appendix B, where the vertices of the Cyclic Polytope are in $2k$ dimensions before being homogenised. Cyclic Polytopes in $2k$ dimensions (even dimension) are rigid: their face structure determines their geometric structure (Cordovil and Duchet 2000, Theorem 5.1). Their geometric structure is that of a Uniform Alternating Oriented Matroid. Any matrix realisation of a Uniform Alternating Oriented Matroid has maximal minors that agree in sign and are non-zero (Cordovil and Duchet 2000, Proposition 3.1) (from the chirotope representation of Oriented Matroids (Björner et al. 1999, Section 9.4)). Any normalisation of the DFT matrix obtained by scaling columns using non-zero scalars does not alter the columnspace of the matrix, and hence the oriented matroid structure is unchanged: the orthants intersected by the columnspace are the same. \square

E DFT Layer as FFT

We can use the FFT to speed up computations, as we will show that computing the logits \mathbf{z} is equivalent to computing the truncated inverse DFT of the input \mathbf{x} , if we reinterpret the vector \mathbf{x} that has $2k + 1$ entries as the coefficients of $k + 1$ complex numbers. Let us start from the inverse DFT, that computes the complex signal in the time domain from the frequency domain. We use n' , d' and k' as variables to avoid confusion with n , d and k , which we have already defined as constants throughout the paper. Denote the complex frequency component for frequency k' by $X_{k'}$ and the signal at time n' by $x_{n'}$, we have:

$$x_{n'} = \sum_{k'=0}^{n-1} X_{k'} \left[\cos\left(\frac{2\pi n'}{n} k'\right) + i \sin\left(\frac{2\pi n'}{n} k'\right) \right] \quad (17)$$

We take the real part of the iDFT, to obtain:

$$\begin{aligned} \text{Re}(x_{n'}) &= \text{Re} \left(\sum_{k'=0}^{n-1} X_{k'} [\cos(k' t_{n'}) + i \sin(k' t_{n'})] \right) \\ &= \text{Re} \left(\sum_{k'=0}^{n-1} (a_{k'} + i b_{k'}) [\cos(k' t_{n'}) + i \sin(k' t_{n'})] \right) \\ &= \sum_{k'=0}^{n-1} [a_{k'} \cos(k' t_{n'}) - b_{k'} \sin(k' t_{n'})] \end{aligned}$$

If we truncate the iDFT to the first k frequencies, we get:

$$\text{Re}(x_{n'}) = \sum_{k'=0}^k [a_{k'} \cos(k' t_{n'}) - b_{k'} \sin(k' t_{n'})]$$

We will now match the coefficients $a_{k'}$ and $b_{k'}$ to corresponding elements in \mathbf{x} (ignoring scaling factors). From the earlier computation of \mathbf{Wx} , we rewrite the logits \mathbf{z} as below:

$$\mathbf{z}_{n'} = \mathbf{w}_{n'}^\top \mathbf{x} \quad (18)$$

$$= \mathbf{x}_1 + \sum_{k'=1}^k [\mathbf{x}_{2k'} \cos(k' t_n) + \mathbf{x}_{2k'+1} \sin(k' t_n)] \quad (19)$$

From which we see that we can write the DFT layer as a truncated Inverse DFT by matching the coefficients of the sines and cosines: $\mathbf{x}_1 = a_0$, $\mathbf{x}_{2k'} = a_{k'}$ and $\mathbf{x}_{2k'+1} = -b_{k'}$. See also our code `test_dft_equivalence.py`. From this perspective, this parametrisation is a low-pass filter.

F Unargmaxable Test Examples

We now introduce two fine-grained measurements of argmaxability, eps -argmaxability and 1-argmaxability. We discuss a few additional insights in the results section below.

F.1 Argmaxability Measurements

eps-argmaxable This is the estimate of argmaxability we can get at the precision of our LP, which is $\text{eps}=10^{-8}$. This roughly means that we can only detect regions which can contain a ball with a radius that is larger than 10^{-8} .

1-argmaxable As we discussed in the paper, some label assignments may be ϵ -argmaxable with a very small ϵ , which makes it hard to predict such label assignments in practice. We therefore also report 1-argmaxability, assuming – by a fairly large margin – that regions with radius 1 are large enough to be easily predicted in practice.

F.2 Results

In Tables 2 to 4 we tabulate the number of argmaxable label combinations on the MIMIC-III, BioASQ and OpenImages v6 test sets. We obtain the following insights.

a) For the DFT, when we make d very small, e.g. $d = 25$, a handful of label combinations in BioASQ are not eps -argmaxable according to the LP. Out of these, one example was found to be infeasible, while for the remaining ones numerical difficulties were encountered by the LP, i.e. Gurobi returned status 12: “*Operation terminated due to unrecoverable numerical difficulties*”. The above issues are likely caused because of dimensionality pressures, the label combinations are ϵ -argmaxable but with a very small ϵ that cannot be detected with the precision of current LPs ($\text{eps}=10^{-8}$, as we discussed in Section 3). This highlights the importance of our proofs, since our results would be tricky to verify using empirical methods alone. Moreover, as we discussed in Section 7, being able to guarantee ϵ -argmaxability with a large ϵ is important future work, since while we showed that our current solution of adding slack variables works in practice, if we increase the pressure on the bottleneck by making d small enough, we can still run into ϵ -argmaxability issues.

b) We note that the behaviour of BSLs in terms of eps -argmaxability and ϵ -argmaxability is quite different when compared to DFT. For BSLs, if a label combination is

argmaxable, it is very often also ϵ -argmaxable. On the other hand, for the DFT some label combinations are argmaxable but are not ϵ -argmaxable, highlighting that the regions do indeed exist, but they can shrink quite a bit in size due to the reduced dimensionality.

Table 2: Median number of ϵ -argmaxable and 1-argmaxable label assignments over 3 random seeds on the dev and test sets of MIMIC-III. **Takeaway: BSL layers have unargmaxable labels starting from $d = 200$ but it does not have to be this way. DFT layers resolve this problem and make all examples argmaxable, but when slack dimensionality is very small, the regions are too small to detect with the precision of the LP.** Note that even if a BSL is able to argmax all test label configurations, this does not imply it will be able to guarantee so for meaningful but unseen future configurations.

split	d	# ϵ -Argmaxable		1-Argmaxable	
		BSL	DFT	BSL	DFT
dev	25	128	1631	128	1572
	50	781	1631	781	1625
	100	1533	1631	1533	1631
	200	1631	1631	1631	1631
	500	1631	1631	1631	1631
test	25	229	3371	229	3216
	50	1515	3371	1515	3356
	100	3137	3371	3137	3370
	200	3370	3371	3370	3371
	500	3371	3371	3371	3371

Table 3: Median number of ϵ -argmaxable and ϵ -argmaxable label assignments over 3 random seeds on the test set of BioASQ. Note that even if a BSL is able to argmax all test label configurations, this does not imply it will be able to guarantee so for meaningful but unseen future configurations.

split	d	# ϵ -Argmaxable out of 10000		# 1-Argmaxable out of 10000	
		BSL	DFT	BSL	DFT
test	25	880	9995	879	8174
	50	6498	10000	6483	9925
	100	9951	10000	9950	10000
	200	10000	10000	10000	10000
	400	10000	10000	10000	10000

G DFT Train Efficiency

Herein we provide more information showing how the DFT layer speeds up convergence and requires less training time to reach equivalent performance. We focus on the most demanding datasets, BioASQ and OpenImages v6, and highlight two perspectives. In Fig. 7, we show how the training loss evolves over time. Meanwhile, in Fig. 8 we compare

Table 4: Median number of ϵ -argmaxable and ϵ -argmaxable label assignments over 3 random seeds on the test set of OpenImages. Note that even if a BSL is able to argmax all test label configurations, this does not imply it will be able to guarantee so for meaningful but unseen future configurations.

split	d	# ϵ -Argmaxable out of 10000		# 1-Argmaxable out of 10000	
		BSL	DFT	BSL	DFT
test	25	2758	10000	2757	9981
	50	8439	10000	8435	10000
	100	9997	10000	9997	10000
	200	10000	10000	10000	10000
	400	10000	10000	10000	10000

the number of hours it took for the BSL and DFT models to converge on BioASQ and OpenImages v6. Both figures show that the DFT layer leads to faster convergence, as it starts training with a lower loss due to the initialisation trick and maintains its lead over the BSL throughout training.

Figure 7: Comparison of BSL and DFT for $d = 100$, in terms of the training cross entropy loss (y-axis, log scale) as training evolves (x-axis). Due to the initialisation trick, the DFT starts training at a lower loss and converges faster.

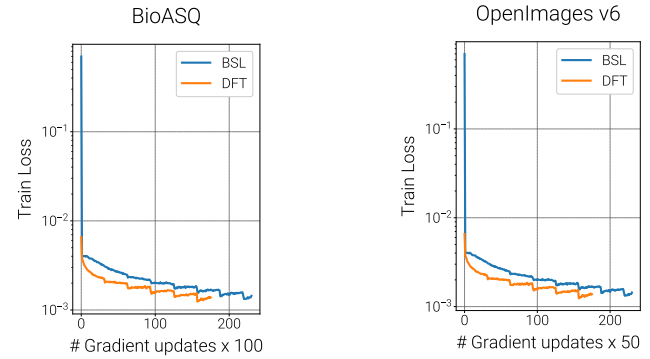
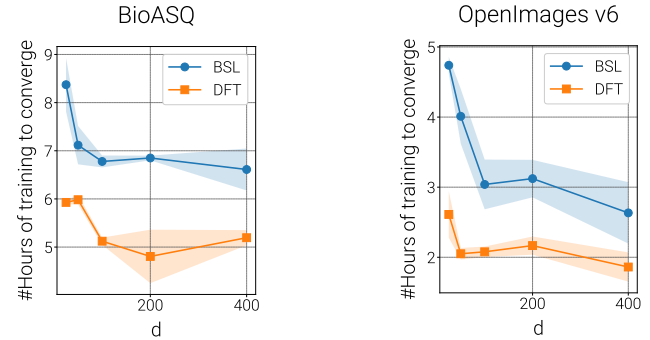


Figure 8: Comparison of BSL and DFT in terms of training time (in hours) to convergence. As can be seen, the DFT converges about 25% faster.



H Reproducibility

H.1 Dataset Access and Preprocessing

MIMIC-III While de-identified, the MIMIC-III dataset (Johnson et al. 2016) contains sensitive and detailed information on the clinical care of patients. As such, permission to access this dataset needs to be requested, as explained here.⁹ We used the same preprocessing, setup and train, validation and test splits as (Mullenbach et al. 2018). See their github repository for more details.¹⁰

BioASQ Task A 2021 The BioASQ Task A dataset (Tsatsaronis et al. 2015; Nentidis et al. 2021) is available after registering for the task on the BioASQ website.¹¹ We created dataset splits which cover $n = 20k$ labels using a 1m subset of the 2021 BioASQ task A dataset. We construct train, validation and test split by sampling examples, making sure that all individual labels (not label combinations) occur in both the train and test sets. We encode the concatenation of the journal, title and abstract as text input. Due to the context size limitation of BERT, we truncate the input to the first 512 subwords. See our code for more details.

OpenImages v6 The OpenImages v6 dataset (Kuznetsova et al. 2020) can be accessed from the project website.¹² We downloaded the images from CVDF, which was linked from the website. Since the dataset is very large, we only used $N = 108228$ images, these had hashes that started with 1 and were available as a single zip download from CVDF. Since the validation and test sets are also large, we validate and test on the first 5k examples of the validation set and the first 10k examples of the test set, correspondingly. For preprocessing, we simply reshape all images to 448x448, as done in Baruch et al. (2020).

H.2 Dataset Statistics

We tabulate the sizes of the dataset splits in Table 5. A histogram of the number of active labels can be seen in Fig. 9.

H.3 Hyperparameters

In order to study the sensitivity of our methods to random initialisation we ran all experiments three times, once per random seed in $(0, 1, 2)$. We train all models using binary crossentropy loss. We summarise all hyperparameters in Table 5. We use early stopping for all models with a patience of 10. The stopping criterion is Prec@8 for MIMIC-III and Validation Loss for BioASQ and OpenImages.

H.4 Training Resources and Train time

We train and evaluate our models on GPUs. For the MIMIC-III dataset we used a NVIDIA 3090 GPU that has 24Gb of RAM and for the remaining two datasets we used an

Figure 9: Comparison of the number of active labels on the training sets of MIMIC-III, BioASQ and OpenImages datasets. All three datasets have a long tail of high cardinality labels, but MIMIC-III has the longest with some examples having more than 60 active labels.



NVIDIA RTX A6000 which has 48Gb of RAM. The experiments took about two weeks of compute. More specifically, the MIMIC-III runs took 9 hours, the OpenImages runs took 85 hours and the BioASQ runs took 188 hours. We verified our models using the LP on CPU on a cluster with an AMD EPYC 7452 32-Core Processor and 500GB of RAM. We parallelised verification by running the LP for each label in parallel to others of the same model. With this setup and running on 50 threads the verification of 10k examples takes from between 20 minutes to 3 hours, depending on the dimensionality (slower for large d).

⁹<https://mimic.mit.edu/docs/gettingstarted/>

¹⁰https://github.com/jamesmullenbach/caml-mimic/blob/master/notebooks/dataproc_mimic_III.ipynb

¹¹<http://participants-area.bioasq.org/>

¹²<https://storage.googleapis.com/openimages/web/index.html>

Table 5: Dataset attributes and model hyperparameters.

	Datasets		
	MIMIC-III	BioASQ task A	OpenImagesV6
n	8921	20000	8933
d	25-400	25-400	25-400
encoder	CNN	PubmedBERT	T-Resnet-L
pretrained	no	yes	yes
encoder dim e	500	768	2432
lr (encoder)	0.001	0.00005	0.0001
lr (classifier)	0.001	0.001	0.001
batch size	16	32	64
patience	10	10	10
eval every epoch	1 epoch	500 steps	250 steps
criterion	P@8	Valid loss	Valid loss
# train	44k	100k	108k
# valid	1.6k	5k	5k
# test	3.3k	10k	10k

I Why DFT Regions Become Very Small

For a matrix \mathbf{W} to have the Uniform Alternating Oriented Matroid structure, all its maximal minors have to be non-zero and have the same sign. Let us assume they are all positive. For the matrix to “robustly” have this structure, the maximal minors should be large, the larger they are the more the row vectors will have to change until two hyperplanes cross and change the Oriented Matroid structure.

However, the DFT matrix is also an orthonormal matrix; all columns have an l_2 -norm of 1 and all pairs of columns have dot product 0. Importantly, an orthonormal matrix $\mathbf{M} \in \mathbb{R}^{n \times d}$, $d < n$ with maximal minors Δ_I indexed by d -subsets of rows, has the property that the sum of squares of the maximal minors is bounded and equals 1:

$$\sum_{I \in \binom{[n]}{d}} \Delta_I(\mathbf{M})^2 = 1 \quad (20)$$

Therefore, we have a bound of 1 on the sum of squares of maximal minors, and since there are $\binom{n}{d}$ maximal minors, a lot of them will have to be very small as we increase the difference between n and d with $d \ll n$.

J Evaluation Metrics

J.1 MLC Metrics

F1 We compute **Micro F1** by computing Precision and Recall across all labels and then computing F1. We compute **Macro F1** by computing Precision, Recall and F1 score for each label individually and then averaging them. Macro F1 does not allow label imbalance to skew the results.

Precision@k (Prec@k) Prec@ k computes the percentage of the k retrieved labels that are indeed correct. We compute the metric by ranking the labels by their assigned probabilities and take the top k as active. We then compute the percentage that is active in the gold data, i.e. we divide the number of correct active labels by k . Prec@ k is not sensitive to the relative ordering of the labels within the top- k .

Recall@ k (Rec@ k) Rec@ k computes how many of the actual active labels are actually retrieved in the top k . As in Prec@ k , we rank the labels by their assigned probabilities and take the top k as active, but this time we divide by the number of labels that are actually active.

F1@ k (F1@ k) As is common with metrics, it is useful to distil as much information as possible into a single number. To achieve this, it is common to use the harmonic mean of Prec@ k and Rec@ k which captures the intuition that we want both Prec@ k and Rec@ k to be high:

$$F1@k = 2 \frac{\text{Prec}@k \text{Rec}@k}{\text{Prec}@k + \text{Rec}@k} \quad (21)$$

Normalised Discounted Cumulative Gain @ k (nDCG@ k) nDCG (Järvelin and Kekäläinen 2002) is sensitive to the relative ranking of examples within the k -top subset, due to the use of discounting. To compute it, we rank the labels according to their assigned probabilities, take the top k and sum their truth values, which for MLC is 1 if the label is active and 0 otherwise. However, as opposed to Prec@ k , DCG@ k adds a logarithmic discount factor such that ranking an irrelevant label above a relevant one is penalised. We use nDCG, which includes normalisation such that the score is in $[0, 1]$, with 1 being optimal.

J.2 More Results

Figure 10: Test set Precision@ k across datasets. For MIMIC-III, Mullenbach et al. (2018) report 58.1 Prec@8 for their CNN baseline. We showed that their result can be improved by: a) Making the learning rate 0.001 b) adding a projection layer after the CNN and c) using the DFT layer.

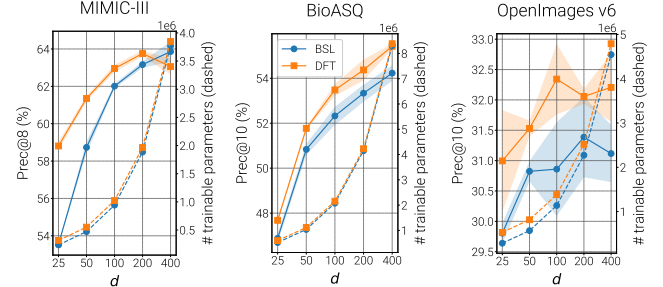


Figure 11: Test set Recall@ k across datasets.

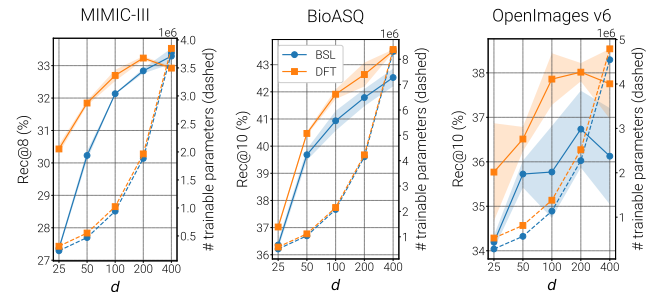


Figure 12: Test set Micro F1 across datasets.

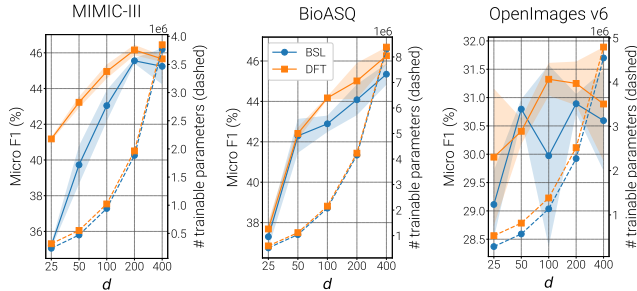


Figure 13: Test set Macro F1 across datasets.

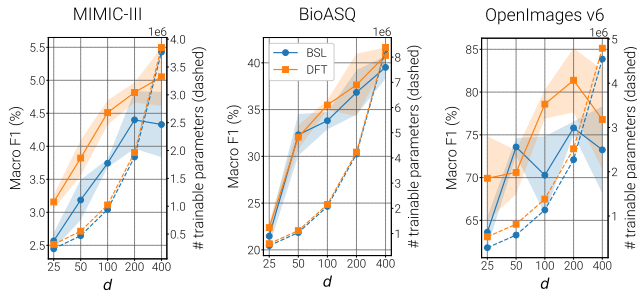
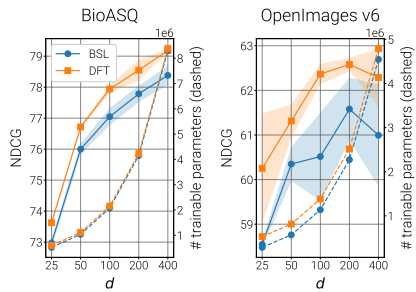


Figure 14: Test set nDCG across datasets.

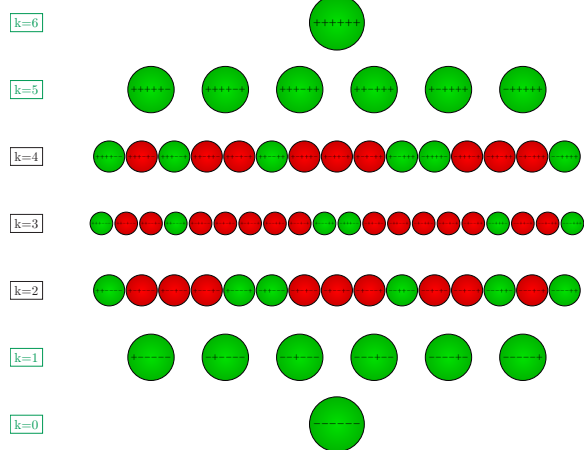


K Illustration of Argmaxable Regions

In the figures to the right, we provide an illustration of the structure of the label assignments for \mathbf{W}^{DFT} . In Fig. 15a, we illustrate the subset of label assignments that are argmaxable. We represent each label assignment as a sign vector where $+$ denotes an active label and $-$ an inactive one. We color the node green if the corresponding label assignment is argmaxable. We can inspect the consequences of Theorem 4 visually, the 1-active label assignments are argmaxable. In Fig. 15b, we illustrate the geometric realisation of \mathbf{W}^{DFT} , where each row of the matrix is a normal vector to a hyperplane. To simplify the plot, instead of plotting the hyperplanes, we plot the Chebyshev balls that correspond to each region. Lastly, in Fig. 15c we show the hyperplanes to make it clearer how the balls in the regions are constructed. For an interactive visualisation see <https://grv.unargmaxable.ai/static/files/alternahedron/index.html>.

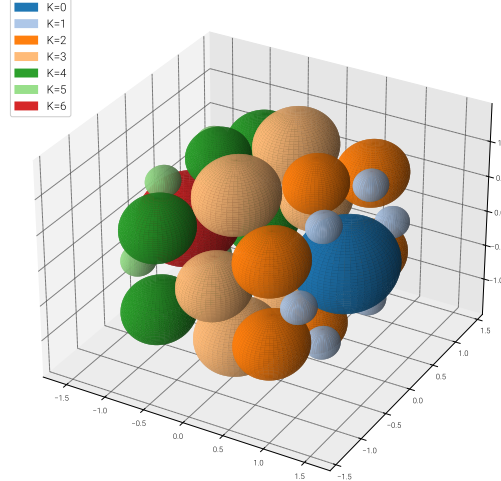
(a) Visual check that for $\mathbf{W} = \mathbf{W}_{6,3}^{\text{DFT}}$ all 2-alternating, and hence all 1-active labels are argmaxable. Each node corresponds to a label assignment, and it is green if it is argmaxable and red if not. We order the labels in levels in terms of k , the number of active labels. As can be seen, the levels for $k = 0$ and $k = 1$ only have green nodes, with unargmaxable label assignments first occurring for $k = 2$.

Enforcing argmaxable 1-active label assignments



(b) Geometric realisation of $\mathbf{W} = \mathbf{W}_{6,3}^{\text{DFT}}$ in 3D space. The 6 hyperplanes defined by the rows of \mathbf{W} tessellate 3D space into 32 regions. For the illustration, we drop the hyperplanes and only plot the Chebyshev regions: each ball is the largest ball that fits in the corresponding region, as discovered by the Chebyshev LP. Each argmaxable label assignment from the plot on the left has a corresponding ball. The six 1-active label assignments from above are the light blue balls, arranged like petals.

Argmaxable regions for Gale(6, 3) K=cardinality



(c) Same plot as above but with hyperplanes drawn.

